Effect of tunable spin-orbit coupling on the superconducting properties of $LaRu_3Si_2$ containing kagome-honeycomb layers

S. Chakrabortty,[1] Ram Kumar,[2,*] and N. Mohapatra[1,†]

[1]*School of Basic Sciences, Indian Institute of Technology Bhubaneswar, Bhubaneswar, Odisha 752050, India*

[2]*Tata Institute of Fundamental Research, Homi Bhabha Road, Colaba, Mumbai 400005, India*

(Received 11 March 2022; revised 28 October 2022; accepted 18 November 2022; published 11 January 2023)

We report a detailed investigation of the superconducting properties of the kagome-honeycomb lattice compound $LaRu_3Si_2$ by systematically tuning the spin-orbit coupling (SOC) via doping of heavier elements Rh and Ir at the Ru site. All doped samples (for a doping level of 10 at. %) preserve the pristine hexagonal crystal structure in the space group $P6_3/mmc$, though a marginal lattice compression was noted for Rh doping. Based on the results of dc magnetization, resistivity, and heat capacity measurements, we derived the normal and superconducting state electronic and thermodynamic properties of the pristine and doped samples. Substitution of Ir/Rh at the Ru site of $LaRu_3Si_2$ resulted in a rather slow but linear suppression of superconducting transition temperature (T_c), which may be related to the decrease in the density of states. As manifested by the estimated electron-phonon (el-ph) coupling constant ($\lambda_{\text{el-ph}} \sim 0.58$–$0.66$) and the normalized specific heat jump at T_c ($\Delta C/\gamma T_c \sim 1.5$), the observed superconductivity in $LaRu_3Si_2$ and the doped variants is moderately coupled. We observed a nonmonotonous variation of the upper critical field [$\mu_0 H_{c2}(0)$] with respect to the doping concentration, as it is influenced by the effective SOC and the coherence length. Most strikingly, we found an enhancement of the superconducting gap parameter ($\Delta_0/k_B T_c$) with doping concentration even though $\lambda_{\text{el-ph}}$ remains essentially unchanged. Moreover, we also notice a nonzero residual electronic specific heat coefficient (γ_r) in the limit $T \to 0$ for all compositions. Interestingly, the evolution of the γ_r with the magnetic field can be well described by a $\sqrt{H}$ dependence, which was attributed to multiband superconductivity.

DOI: 10.1103/PhysRevB.107.024503

I. INTRODUCTION

The kagome lattice is one of the most sought after electronic systems, which has garnered a great deal of attention as a unique platform for the realization of exotic quantum states of matter [1–5]. A variety of unconventional electronic and magnetic instabilities have been reported at different electron filling levels of these states [5–7]. Conventionally, it was believed that the insulating variants of kagome systems with antiferromagnetically coupled spins are manifested by high degrees of geometric frustration, and these systems are extremely attractive as potential hosts to the quantum spin-liquid states [7–9]. However, subsequently, it was shown that metallic kagome systems also present an interesting scenario owing to similar geometric confinement [10,11]. Additionally, kagome metals host unique electronic features with a combination of Dirac-type bands and dispersionless flat bands, which encompass emergent topological properties including massive Dirac fermions and nontrivial Berry phase [3,12,13]. Recent studies on the kagome ferromagnets Fe_2Sn_3 and $Co_3Sn_2S_2$ have shown noteworthy observation of spin-degenerate Dirac bands, two-dimensional Chern gap, large anomalous Hall conductivity, and magnetic Weyl excitations [4,13–16]. Moreover, theoretical studies also suggest kagome systems have the ability to support phenomena such as charge fractionalization [17], unusual magnetism [15], correlated topological states [18], and superconductivity [6,19]. Specifically, the realization of the superconducting ground state in the backdrop of such electronic and magnetic fluctuations may be associated with some unusual mechanism or quasiparticles. However, very few metallic systems with kagome layers are known to exhibit superconductivity. Prominent examples include 132-type RT_3Si_2/RT_3B_2 (R = La, Ce, and Th; T = Ru, Rh, Ir, and Os) [20–24] and the recently discovered family 135-type AV_3Sb_5 (A = K, Rb, and Cs) [25–27]. The superconductivity in the 135-type system is shown to be unconventional with Z_2 topology in the normal state [19,28]. It has also been predicted that the superconductivity in these systems originates from nesting-driven interactions in the Fermi surface [19,25]. On the other hand, this mechanism is not applicable for the 132-type system, as the electronic structure calculations results on $LaRu_3Si_2$ revealed the absence of any strong nesting effect in the Fermi surface [24]. Also, the calculated band structure of $LaRu_3Si_2$ possesses a flat band and Dirac-like band formed by the Ru-d_z^2 bands near the Fermi level [29]. Furthermore, it has been shown that all five 4d Ru orbitals contribute to conduction and superconductivity. A similar situation has also been reported for Fe in iron-pnictide superconductors, which indicates the role of correlation effects [30]. Preliminary studies on the

*Current address: Maryland Quantum Materials Center and Department of Physics, University of Maryland, College Park, Maryland, USA.

†niharika@iitbbs.ac.in

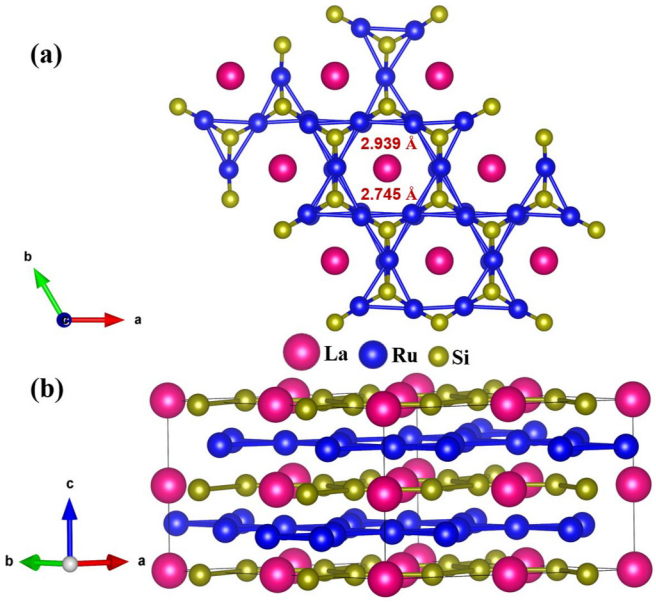

FIG. 1. A schematic view of the hexagonal structure of $LaRu_3Si_2$ (a) in the *ab* plane and (b) along the *c* axis. The Ru atoms construct a distorted kagome lattice structure, while the Si and La atoms form a honeycomb and a triangular structure, respectively. The Ru-Ru bond length varies alternatively between 2.94 and 2.75 Å.

superconducting properties of $LaRu_3Si_2$ based on the results of La-NQR measurements claim *s*-wave superconductivity with strong electron-phonon interaction ($\lambda_{\text{el-ph}}$) and a large energy gap [$2\Delta(0) \sim 5.5\, k_B T_c$] [31]. However, the estimated value of $\lambda_{\text{el-ph}}$ by McMillan's formula using the Debye temperature is comparatively low and did not corroborate the large energy gap. Moreover, a sharp coherence peak was reported just below T_c, while it is generally expected that a strong electron-phonon coupling would suppress the coherence peak due to the large lifetime of the quasiparticles. Additionally, recent experimental studies of the heat capacity and magnetic properties of $LaRu_3Si_2$ revealed anomalous behavior of the induced quasiparticle density of states in the superconducting states attributed to the strong correlation effect [24]. Though the results of μSR measurements indicate a single isotropic *s*-wave type gap function with intermediate coupling, the phonon-mediated pairing mechanism is not sufficient to explain the superconducting state of $LaRu_3Si_2$. Therefore, additional experimental and theoretical studies are necessary to get more insight into the pairing mechanism and related gap structure of this material.

The material, $LaRu_3Si_2$ crystallizing in a hexagonal structure with space group $P6_3/mmc$, has interesting crystallographic features with a unique combination of the isolated layers of kagome and honeycomb networks. As shown in Fig. 1(a) , the Ru atoms are arranged at the vertices of corner-sharing triangles but of two different side lengths, forming a distorted kagome layer in the *ab* plane. These kagome layers are sandwiched between the La-Si honeycomb layers [see Fig. 1(b)]. Due to the distortion in the kagome layer, the *c* axis of these compounds is doubled compared with that of the undistorted one. This feature distinguishes $LaRu_3Si_2$ from other members of the 132-type family and hence exhibits the highest T_c among this family of compounds. The Ru-Ru bond lengths within the plane (2.76 and 2.98 Å) are comparable with the atomic separation in the elemental Ru, but the out-of-plane bond length is much higher (3.57 Å). These structural features are expected to result in a dominating two-dimensional conducting behavior with large spin fluctuations. However, band structure calculations have shown strong hybridization of Ru and Si orbitals giving rise to a three-dimensional Fermi surface. Moreover, the structure also contains interfacial honeycomb layers of Si with La atoms arranged in triangular fashion. Honeycomb layered structures such as graphene and AlB_2 derived ternary compounds are attracting a lot of interest due to their electronic and magnetic characteristics including superconductivity [32–34].

We believe that the impurity-induced pair-breaking effects and suppression of T_c can be a route for understanding the gap symmetry and pairing mechanism. It was shown that superconductors with different types of pairing symmetry respond to the addition of impurities in a specific way. For example, the substitution of any nonmagnetic impurity in a conventional single-band *s*-wave superconductor registers no change in T_c and pairing interaction, while magnetic impurities suppress superconductivity rapidly [35,36] due to exchange interaction of the local spin of the impurity site with conduction electrons of the host [37]. However, in a *d*-wave superconductor such as cuprates, nonmagnetic (scalar) impurities can also cause the change of phase and gap amplitude of the nontrivial pairing states [36,37] like the magnetic ones, and thereby, both magnetic and nonmagnetic impurities suppress T_c rapidly [37,38]. Analogous to the *d*-wave superconductors, the $s^{\pm}$-wave pairing state of iron-chalcogenide superconductors is equally sensitive to magnetic and nonmagnetic impurities, though the results are highly controversial and material specific [39,40].

In this regard, we find that the suppression of T_c by doping at the La or Ru site in $LaRu_3Si_2$ is distinct from both *s*- and *d*-wave pairing states. With partial substitution of Tm or Gd at the La site, T_c was reduced at a very slow rate (∼1.3 K for 5% of Gd doping and ∼1.4 K for 16% of Tm doping), indicating that superconductivity in this system is robust against the paramagnetic centers [41,42]. Similarly, the doping of transition metals (Co, Ni, and Cr) at the Ru site also resulted in a gentle drop in T_c. Interestingly, however, the substitution of only 3% Fe at the Ru site completely suppressed superconductivity in this system [43]. Such an exceptional reduction of T_c with Fe doping was explained on the basis of higher moment formation per Fe dopant (1.4 μ_B/Fe) in comparison with that of other transition metals Co, Ni, or Cr (∼0.6–0.8 μ_B/dopant) [43,44]. Another school of thought was developed by Wang *et al.* [45] based on the phenomenological multiband impurity scatterings, which were also extended to include gap anisotropy. This shows a correlation between the residual resistivity with the rate of suppression of T_c. In contrast to this proposal, it has been shown that the residual resistivity of doped $LaRu_3Si_2$ samples increases at a much higher rate with a Co dopant than a Fe dopant [43], and therefore, this concept is certainly not applicable to $LaRu_3Si_2$.

In this paper, we investigate the magnetic and transport properties of the solid solutions $La(Ru_{1-x}M_x)_3Si_2$ with M = Rh and Ir to gain insight into the role of spin-orbit cou-

pling (SOC) on the upper critical field, rate of suppression of T_c, electron-phonon (el-ph) coupling strength, and the superconducting gap structure. An extensive analysis of the resistivity, magnetic susceptibility, and heat capacity results shows the influence of SOC and disorder for the variation of H_{c2} in the doped samples, while the el-ph coupling strength remains essentially unaffected by doping. Moreover, the field-dependence of electronic specific heat in the superconducting states of the doped samples indicates the multiband effects.

II. EXPERIMENTAL DETAILS

Polycrystalline samples of $La(Ru_{1-x}Ir_x)_3Si_2$ and $La(Ru_{1-y}Rh_y)_3Si_2$ (with x, $y = 0$, 0.05, and 0.1) were synthesized by a conventional arc-melting process on a water-cooled copper hearth in a high-purity argon atmosphere with Ti as a getter. The high-purity raw materials, elemental La, Ru, Si, Rh, and Ir pieces, were weighed out maintaining a stoichiometric ratio of La : $(Ru_{1-x}Ir_x)/(Ru_{1-y}Rh_y)$: Si as 1:3.45:2 for melting. An extra amount of Ru (15% more) is essential to avoid the formation of the $LaRu_2Si_2$ phase [24]. To ensure homogeneity, all ingots were remelted at least 4–5 times by flipping upside down each time. The weight loss after the final melting was found to be negligible (<1%). The phase identification and structural characterization of the samples were done by x-ray diffractometry. Powder x-ray diffraction (PXRD) patterns of all synthesized samples were collected at room temperature using a Bruker D8 ADVANCE diffractometer equipped with CuKα radiation. Moreover, the morphology and atomic composition of the grains were determined by field emission scanning electron microscopy (FESEM), attached with an energy-dispersive x-ray (EDX) spectroscopy study. Measurements of temperature (T)- and magnetic field (H)-dependent magnetization were performed in a vibrating sample magnetometer attached to the commercial physical property measurement system (PPMS; Dynacool, Quantum Design). The resistivity and specific heat measurements were also carried out with the same PPMS. Standard four-point contacts with silver paint on rectangular-shaped samples were used for the electrical resistivity measurements, while a small, flat bulk sample was used for the specific heat measurements by the time-relaxation method.

III. RESULT AND DISCUSSION

A. Structural characterization

Figure 2(a) shows the PXRD patterns of all samples at room temperature. Rietveld refinement of the XRD data was executed by the FULLPROF (WinPlotr) software package [46], and the calculated patterns are also displayed along with the measured data. It is apparent from the analysis that most of the diffraction peaks in the pattern can be well indexed to the hexagonal structure in space group symmetry $P6_3/mmc$. Additionally, weak impurity peaks, from the extra Ru, were detected, which were also included in the refinement process. By expanding the 2θ regions around the (220) peak, as shown in Fig. 2(b), one may notice an apparent shift toward the higher angle side with increasing the doping concentration of Rh, while it is less obvious with Ir concentration. This may

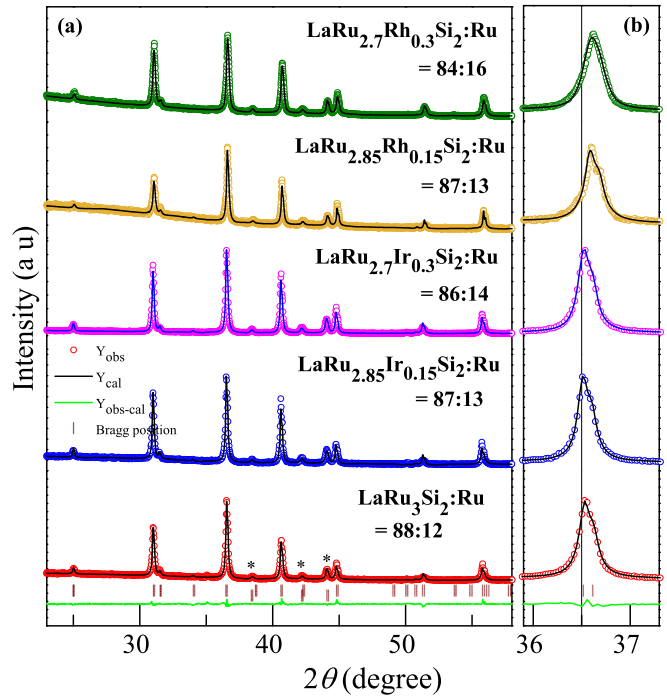

FIG. 2. X-ray diffraction pattern and Rietveld refinement of (a) $La(Ru_{1-x}Ir_x)_3Si_2$ ($x = 0$, 0.05, and 0.1) and $La(Ru_{1-y}Rh_y)_3Si_2$ ($y = 0$, 0.05, and 0.1). (b) An enlarged view of the (200) peak showing an apparent shift toward the higher angle side with doping.

be understood based on the difference in the ionic radii of Rh^{4+} and Ru^{4+} and nearly similar radii of Ru^{4+} and Ir^{4+}. The lattice constants and other structural parameters obtained from the refinement results are summarized in Table S1 in the Supplemental Material [47]. The values of the lattice constants of the parent compound are in good agreement with those previously reported on $LaRu_3Si_2$ [24,42]. Moreover, we recorded a systematic decrease in both the lattice parameters by Rh substitution, suggesting the development of a small positive pressure on the kagome layer of the lattice. On the other hand, a marginal increase in the unit cell volume was observed for the Ir-doped samples.

The microstructural analysis of all samples was performed by collecting FESEM images of the arc-melted samples. The morphology of all samples shows fused grains without noticeable grain boundaries. Elemental mapping of all the individual atoms suggests uniform distribution (see Fig. S1, Supplemental Material) [47]. The chemical composition of the samples was estimated by EDX spectra collected at several locations of the sample, and the average value (as shown in Fig. S1, Supplemental Material) [47] confirms that the weight percentage of constituent elements corresponds to the desired stoichiometry within the experimental error.

B. Magnetic properties

The superconducting properties of the doped samples were first characterized by the measurement of temperature-dependent magnetization under zero-field-cooled (ZFC) and field-cooled (FC) conditions of the specimen sample. Figures 3(a) and 3(b) present the volume susceptibility vs

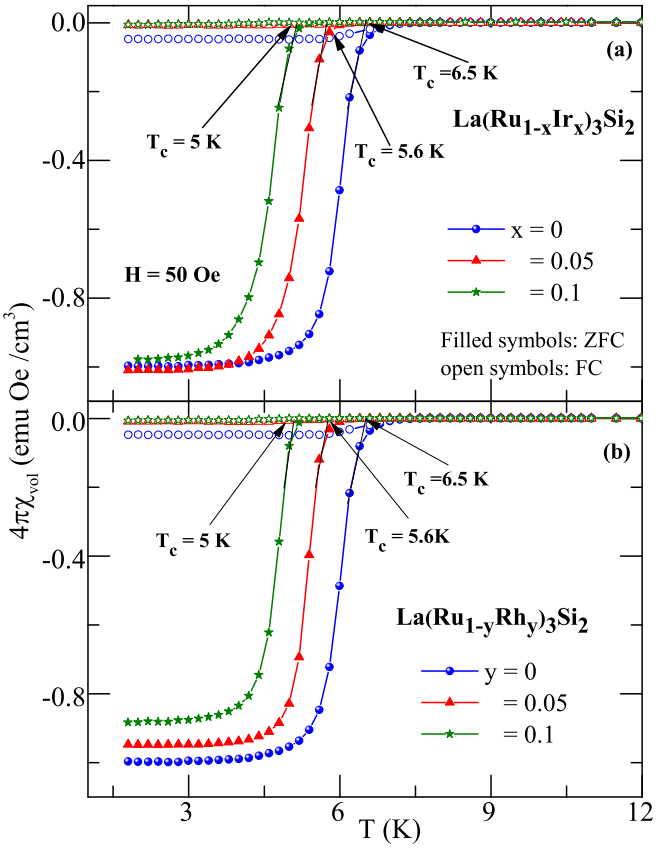

FIG. 3. Temperature dependence of dc magnetic susceptibility of (a) $La(Ru_{1-x}Ir_x)_3Si_2$ ($x = 0$, 0.05, and 0.1) and (b) $La(Ru_{1-y}Rh_y)_3Si_2$ ($y = 0$, 0.05, and 0.1) in zero-field-cooled and field-cooled modes under an applied field of 50 Oe.

temperature of the pristine and the doped samples in an applied field of 5 mT. The ZFC susceptibility was corrected for the demagnetization factor $\mathcal{N} = 0.05$–0.15 (obtained from the $M(H)$ data, as discussed in the Supplemental Material [47]; see also Refs. [48,49] therein), using the following expression: $\chi = \frac{\chi_{exp}}{1-\mathcal{N}\chi_{exp}}$ [48]. At 2 K, χ_{ZFC} approaches the diamagnetic signal close to $-\frac{1}{4}\pi$, indicating bulk superconductivity of ~100% volume fraction for all doped samples. Moreover, the divergence of ZFC and FC susceptibilities demonstrates strong flux line pinning characteristics of all samples studied. The onset temperature of the superconducting state was determined from the intersection between the extrapolated curves corresponding to the superconducting and normal state susceptibilities [50], which shows a systematic decrease of T_c from 6.5 to 5.0 K for a doping concentration of 10% of Ir or Rh. It is worthwhile to mention that the T_c of the parent compound agrees well with the previous literature [29]. Interestingly, an upturn feature observed in the ZFC and FC magnetization of the parent compound immediately before the superconducting transition [42] is completely suppressed in the doped samples.

To further characterize the superconducting states and determine the upper and lower critical fields, magnetization was measured as a function of the magnetic field at several temperatures in the range 1.8–10 K. Figure 4(a) depicts the enlarged view of low field magnetization data of $LaRu_{2.7}Ir_{0.3}Si_2$, while

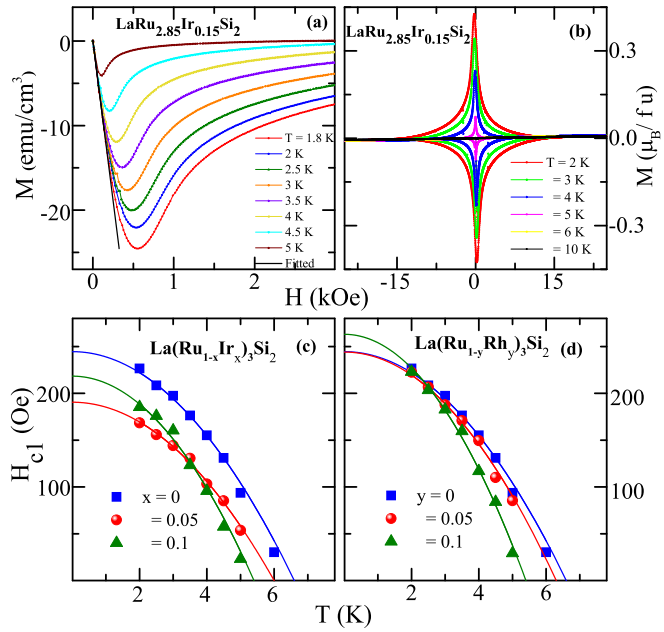

FIG. 4. The isothermal *M*-*H* curve at several temperatures ranging from 1.8 to 10 K for $LaRu_{2.85}Ir_{0.15}Si_2$ (a) in the low field range and (b) in the extended field range. (c) and (d) Variation of H_{c1} with temperature for $La(Ru_{1-x}Ir_x)_3Si_2$ and $La(Ru_{1-y}Rh_y)_3Si_2$, respectively.

the magnetic hysteresis loops are shown in Fig. 4(b). The magnetization behavior of all other samples shows similar features which are typical of a type-II superconductor. By following a criterion frequently used in the literature [48], we estimated the value of the lower critical field ($\mu_0 H_{c1}$) from the low field (ZFC) $M(H)$ behavior. The field at which $M(H)$ deviates from linearity by 1% ($\mu_0 H_{c1}^{ex}$) is further subjected to a demagnetizing correctional factor to obtain $\mu_0 H_{c1}$ at each temperature [$\mu_0 H_{c1} = \mu_0 H_{c1}^{ex}/(1-\mathcal{N})$] [51,52], where $\mathcal{N}$ is the demagnetizing factor [the detailed analysis of M vs H data along with the determination of $\mathcal{N}$ is shown in the Supplemental Material [47]. In Figs. 4(c) and 4(d), the resulting $\mu_0 H_{c1}$ values are plotted as a function of temperature for all doped samples and compared with that of the pristine. According to the Ginzberg-Landau (GL) theory of phase transition, $H_{c1}(T)$ can be modeled by the relation as follows [53]:

$$H_{c1}(T) = H_{c1}(0)\left[1 - \left(\frac{T}{T_c}\right)^2\right]. \quad (1)$$

The solid line through the data points in Figs. 4(c) and 4(d) shows good agreement of the GL theory and provides us the $\mu_0 H_{c1}(0)$ values as 24.1 ± 0.4 mT, 19.1 ± 0.2 mT, and 21.8 ± 0.6 mT for the parent, 5%, and 10% Ir-doped samples, respectively. A similar analysis of the magnetization data of Rh-doped samples yields the lower critical fields as 24.4 ± 0.3 mT and 26.3 ± 0.5 mT for 5% and 10% Rh-doped samples. A glance at these numbers reveals an enhancement of the reduced lower critical field $\mu_0 H_{c1}(0)/T_c$ with doping.

C. Electrical resistivity

The temperature dependences of zero-field electrical resistivity of $La(Ru_{1-x}Ir_x)_3Si_2$ and $La(Ru_{1-y}Rh_y)_3Si_2$ measured

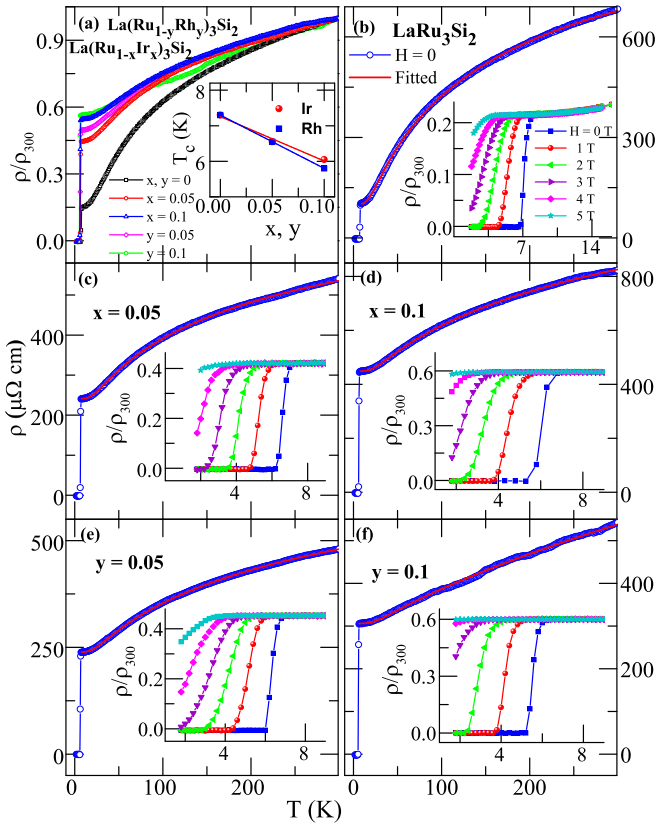

FIG. 5. (a) Temperature dependence of normalized resistivity of $La(Ru_{1-x}Ir_x)_3Si_2$ ($x = 0$, 0.05, and 0.1) and $La(Ru_{1-y}Rh_y)_3Si_2$ ($y = 0$, 0.05, and 0.1). Inset shows the variation of T_c with Ir/Rh concentration. (b)–(f) Temperature dependence of the zero-field resistivity of $LaRu_3Si_2$ and the doped samples, respectively. The solid red line represents the fit of the parallel resistor model (as described in the text). The inset of the graph in (b)–(f) demonstrates the gradual shifting of the superconducting transition temperature with a magnetic field in the range 0–5 T.

in the T range of 1.8–300 K are presented in Fig. 5(a). For a better comparison of the T-dependent features, we have shown the normalized resistivity data to the value obtained at 300 K. All samples exhibit a metallike decrease of resistivity with temperature ($d\rho/dT > 0$) and then a sharp transition to zero resistive states at low temperature, signifying the onset of superconductivity. The transition is comparatively broader, spreading over a temperature width of ∼1 K like that of the parent compound, which has been attributed to the superconducting fluctuations [24]. Defining the T_c value as the midpoint of this resistivity drop (i.e., 50% criterion was used to determine T_c,), one may see a monotonic decrease of T_c with x for both Rh and Ir concentration. Comparing the observed suppression of T_c with the previous reports [43,44], it may be stated that the rate of change of T_c by Rh/Ir doping is higher than that of Co doping but much lower than that of Fe doping. In addition to the decrease in T_c, the normal state resistivity behavior undergoes a substantial variation. The residual resistivity (ρ_0) systematically increases, while the residual resistivity ratio (RRR $= \rho_0/\rho_{300}$) gradually decreases by increasing the dopant concentration (Rh/Ir), presumably due to the enhancement of the electron scattering by lattice distortion or defect centers induced by doping. Moreover, it may be noticed that the pronounced negative curvature seen in the high temperature $\rho(T)$ of the pristine gets flattened for the doped samples. Such a trend of $\rho(T)$ behavior is analogous to that of Co doping and in contrast to that of Fe doping [43]. Several other superconductors such as Nb_2PdS_5 [54], $Mo_{1-x}Re_xTe_2$ [55], and Zr_5Ge_3 [56] also exhibit a similar trend in their $\rho(T)$ behavior upon metal-site doping.

To evaluate the electronic correlations and scattering mechanisms at low temperatures, i.e., in the normal state just above T_c, we used the power law relation as shown below to fit the resistivity data:

$$\rho(T) = \rho_0 + AT^n, \tag{2}$$

where ρ_0 is the residual resistivity, A is the coefficient to be determined, and n the exponent. From the best fit (see Fig. S2 in the Supplemental Material [47]) we obtained the value of n (which is used as a free parameter during fitting) as 2 ± 0.1 for all samples studied here. This quadratic temperature dependence of resistivity just above the superconducting transition reflects the dominance of the el-el scattering mechanism assuring the Fermi liquid description in this T range [57]. Furthermore, the electronic correlation can be qualitatively understood by analyzing the Kadowaki-Woods ratio, defined as A/γ^2 (where A is the coefficient of the T^2-dependent term and γ the coefficient of electronic specific heat). The obtained values of A/γ^2, as shown in Table I, are of the order of a_0 (1.0×10^{-5} $\mu\Omega$ cm mole K^2 mJ^{-2}) which is mostly found for many heavy fermion compounds [58]. It may be seen that there is an overall decrease in this ratio and in turn the electronic correlations by doping, while the change is not linear in case of Ir doping. The reason for this behavior of Ir-doped samples is not clear to us at this moment.

At higher temperatures ($T > 50$ K), there is a significant deviation from this Fermi liquid behavior because of stronger el-ph scatterings, which is found to be different at different doping levels. For a quantitative analysis of the el-ph scatterings, we used a parallel resistor (PR) model that describes the resistivity behavior with a tendency to saturate at higher temperatures [59]. Such a characteristic manifests the Ioffe-Regel limit at which the mean free path is comparable with the interatomic spacing, leading to a high absolute resistivity value. A brief discussion on the PR model and the fitting results are presented in the Supplemental Material (Table S2) [47] (see also Refs. [60–62] therein). As illustrated in Figs. 5(b)–5(f), the experimental data show excellent agreement with the PR model in the high-temperature limit, suggesting that the carriers are primarily scattered by longitudinal acoustic phonons. Therefore, the electron-phonon coupling constant can be determined from the Debye temperature.

To estimate the upper critical field corresponding to the superconducting state of the pristine and doped samples, we examined the temperature-dependent resistivity with various applied fields, and the results are displayed in the insets of Figs. 5(b)–5(f). The emergence of resistivity with the application of magnetic field is rather slow, yielding a high upper critical field $\mu_0 H_{c2}(0)$. Figure 6 shows the variation of $\mu_0 H_{c2}$ as a function of the reduced temperature ($t = T/T_c$). By fitting the empirical formula [Eq. (3)] with the extracted data, we

TABLE I. Specific heat coefficients and Kadowaki-Woods ratio derived from the normal state specific heat and resistivity of $La(Ru_{1-x}Ir_x)_3Si_2$ ($x = 0$, 0.05, and 0.1) and $La(Ru_{1-y}Rh_y)_3Si_2$ ($y = 0$, 0.05, and 0.1).

Sample	γ(mJ mole^{-1} K^{-2})	β(mJ mole^{-1} K^{-4})	δ(mJ mole^{-1} K^{-6})	A/γ^2 ($\mu\Omega$ cm mole^2 K^2 mJ^{-2})
$LaRu_3Si_2$	33.3 ± 0.2	0.14 ± 0.01	0.004 ± 0.0001	6.82×10^{-5}
$LaRu_{2.85}Ir_{0.15}Si_2$	29.9 ± 0.1	0.24 ± 0.01	0.003 ± 0.00005	3.86×10^{-5}
$LaRu_{2.7}Ir_{0.3}Si_2$	25.2 ± 0.1	0.34 ± 0.004	0.0022 ± 0.00003	5.23×10^{-5}
$LaRu_{2.85}Rh_{0.15}Si_2$	29.0 ± 0.2	0.47 ± 0.01	0.0025 ± 0.0001	2.93×10^{-5}
$LaRu_{2.7}Ir_{0.3}Si_2$	25.5 ± 0.2	0.20 ± 0.01	0.0027 ± 0.0001	2.21×10^{-5}

obtained $\mu_0 H_{c2}(0)$ for the pristine and the doped samples:

$$H_{c2}(T) = H_{c2}(0)\left[\frac{1-t^2}{1+t^2}\right]. \quad (3)$$

The resultant $H_{c2}(0)$ values are listed in Table II. One may notice an enhancement of $H_{c2}(0)$ for the smaller doping level (5%) [5.13 and 4.61 T for Ir- and Rh-doped samples, respectively] with respect to that for the pristine (3.96 T), while it reduces by further increasing the doping concentration. It is trivial to assume an overall increase in the spin-orbit scattering parameter due to the doping of heavier element Ir/Rh substituting Ru, which might be causing an enhancement of $H_{c2}(0)$. However, the nonmonotonous trend of $H_{c2}(0)$ against the doping concentration indicates the role of some other mechanism. Since the upper critical field [$\mu_0 H_{c2}(0)$] is inversely proportional to the square of effective coherence length of the superconducting state, such an effect may also arise due to a decrease in the effective coherence length because of doping. In fact, we also observe a systematic increase in the residual resistivity (ρ_0) and in turn a decrease of the mean free path with doping. However, $\mu_0 H_{c2}(0)$ does not show linear dependence on the doping concentration (x or y) even though l_e decreases monotonously with both Rh and Ir doping. Therefore, spin-orbit interaction also has significant influence for the enhancement of $\mu_0 H_{c2}(0)$ in addition to the effective coherence length. A similar effect has been reported for Nb_2PdS_5 when doped with the heavier element Pt replacing Pd [54].

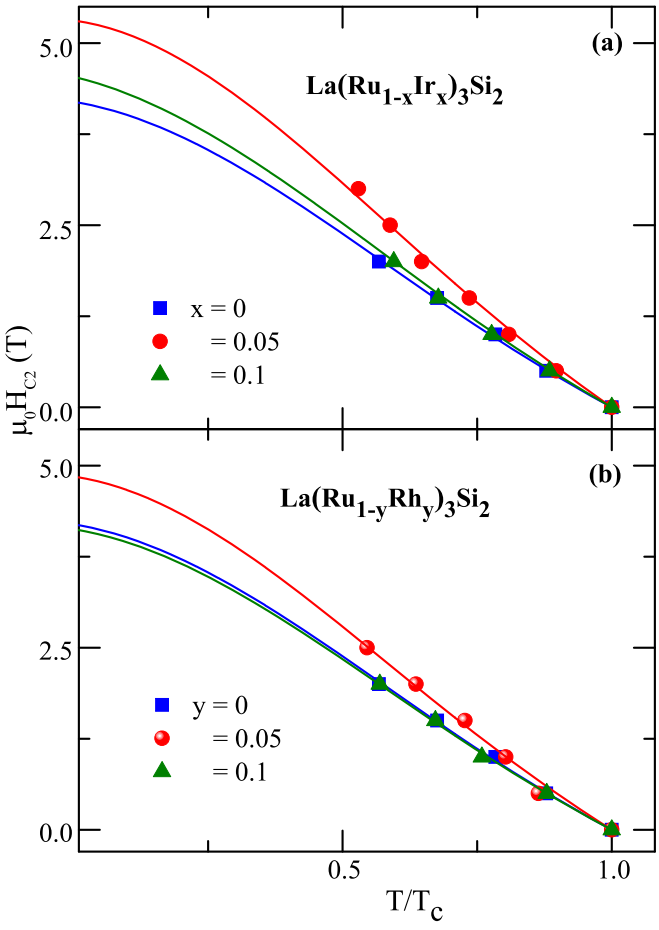

FIG. 6. Variation of H_{c2} with temperature derived from the resistivity measurements of (a) $La(Ru_{1-x}Ir_x)_3Si_2$ ($x = 0$, 0.05, and 0.1) and (b) $La(Ru_{1-y}Rh_y)_3Si_2$ ($y = 0$, 0.05, and 0.1). The solid line through the data points corresponds to the empirical formula [Eq. (3)] as discussed in the text.

In type-II superconductors, the suppression of superconductivity under the application of a magnetic field can be understood by two different mechanisms based on two different magnetic channels which affect the superconducting state. The most common pair-breaking effect occurs via the orbital limiting effect due to the Lorentz force which signifies a higher kinetic energy with respect to the condensation energy of the Cooper pairs. Alternatively, if the Pauli spin susceptibility energy exceeds the condensation energy, the pair-breaking mechanism is attributed to the spin paramagnetic effect. When both effects contribute, the temperature dependence of the upper critical field can be described by the Werthamer-Helfand-Hohenberg (WHH) theory which includes the influence of Pauli spin paramagnetism as well as the spin-orbit interaction. As shown in Fig. 6, the upper critical field at low field limit or temperatures just below T_c varies essentially linearly with T, yielding a slope ($d\mu_0 H_{c2}/dT$) of (−0.65 T/K) for $x(y) = 0$, −0.95 (−0.83) T/K, and −0.75 (−0.72) T/K for $x(y) = 0.05$ and $x(y) = 0.1$, respectively, for Ir (Rh)-doped samples. This implies that the resulting orbital limiting critical fields can be derived by using the WHH equation (in the absence of Pauli spin paramagnetism and the spin-orbit interaction) as follows [63,64]:

$$H_{c2}^{\mathrm{orb}}(0) = -AT_c\frac{dH_{c2}(T)}{dT}, \quad (4)$$

where A is the purity factor and takes the value 0.693 (0.73) for superconductors in the dirty (clean) limit. Considering the dirty limit condition (discussed in the later section), we obtained the $H_{c2}^{\mathrm{orb}}(0)$ values as 3.29 T, 4.31 (3.77) T, and 3.14 (2.89) T for $x(y) = 0$, 0.05, and 0.1, respectively, for Ir (Rh)-doped samples. On the other hand, the Pauli-limiting upper

TABLE II. Superconducting properties of $La(Ru_{1-x}Ir_x)_3Si_2$ and $La(Ru_{1-y}Rh_y)_3Si_2$ ($x, y = 0$, 0.05, and 0.1) extracted from the experimental results. The extracted parameters $H_{c1}(0)$, $H_{c2}(0)$, $H_{c2}^{orb}(0)$, $\xi_{GL}(0)$, $\lambda_{GL}(0)$, $H_c^{cal}(0)$, and $H_c^{ex}(0)$ are determined from Eqs. (1), (3), (4), (15), (16), (18), and (21), respectively.

Sample→		$La(Ru_{1-x}Ir_x)_3Si_2$			$La(Ru_{1-x}Rh_x)_3Si_2$	
Parameters↓	Unit↓	$x = 0$	$x = 0.05$	$x = 0.1$	$y = 0.05$	$y = 0.1$
T_c	K	7.3	6.55	6.05	6.55	5.8
$H_{c1}(0)$	mT	24.5 ± 0.3	19.1 ± 0.2	21.8 ± 0.4	24.4 ± 0.27	26.3 ± 0.5
$H_{c2}(0)$	T	3.97 ± 0.05	5.13 ± 0.08	4.21 ± 0.04	4.61 ± 0.01	3.90 ± 0.04
$H_{c2}^{orb}(0)$	T	3.29 ± 0.01	4.31 ± 0.03	3.14 ± 0.01	3.77 ± 0.4	2.89 ± 0.01
$H_{c2}^{P}(0)$	T	13.50	12.12	11.19	12.12	10.73
α_M		0.34 ± 0.005	0.50 ± 0.006	0.39 ± 0.004	0.49 ± 0.06	0.34 ± 0.001
$\xi_{GL}(0)$	nm	9.1 ± 0.06	8.01 ± 0.06	8.9 ± 0.04	8.5 ± 0.01	9.2 ± 0.04
$\lambda_{GL}(0)$	nm	135 ± 1	161 ± 1	145 ± 1	137 ± 1	129 ± 2
$H_c^{cal}(0)$	mT	190 ± 2	181 ± 3	181 ± 2	201 ± 3	197 ± 2
$H_c^{ex}(0)$	mT	263.1 ± 23	202.3 ± 12	156.5 ± 18	219.6 ± 15	173.1 ± 9
ξ_{BCS}	nm	26.2 ± 0.56	23.44 ± 0.5	19.86 ± 0.4	22.89 ± 0.6	20.17 ± 0.07

critical fields can be calculated by following the Bardeen-Cooper-Schrieffer (BCS) formalism $H_{c2}^{P}(0) = 1.85\ T_c$. With the estimated T_c from the resistivity curves as described above, we derived the $H_{c2}^{P}(0)$ values as 13.50, 12.12, and 11.19 T for $La(Ru_{1-x}Ir_x)_3Si_2$ ($x = 0$, 0.05, and 0.1) and 12.12 and 10.73 T for $La(Ru_{1-y}Rh_y)_3Si_2$ ($y = 0.05$ and 0.1).

It is apparent from the above analysis that the values of $H_{c2}^{orb}(0)$ are comparatively smaller than the upper critical fields [$H_{c2}(0)$] obtained from the empirical formula [Eq. (3)] but remains well below the Pauli paramagnetic limiting fields $H_{c2}^{P}(0)$ for all doped samples including the pristine, indicating the dominance of the orbital pair-breaking mechanism in these systems. To further estimate the significance of spin paramagnetic effects, we calculated the Maki parameter (α_M) which is defined in the following expression:

$$\alpha_M = \sqrt{2}\frac{H_{c2}^{orb}(0)}{H_{c2}^{P}(0)}. \quad (5)$$

The estimated values of α_M are 0.34, 0.50, and 0.39 corresponding to the doping concentration $x = 0$, 0.05, and 0.1 for Ir and are 0.49 and 0.34 corresponding to $y = 0.05$ and 0.01 for Rh-doped samples, respectively. Though the relative size of the Maki parameter suggests little influence of the Pauli paramagnetic field, the variation of α_M with doping may arise due to the interplay of the spin-orbit interaction and disorderness caused by doping.

To get more insight into the effect of the spin-orbit interaction and Pauli paramagnetism, we tried to simulate the $\mu_0 H_{c2}(T)$ behavior in the entire temperature region below T_c by using the one-band WHH model, which allows us to estimate $\mu_0 H_{c2}(0)$ considering the effects of Pauli spin paramagnetism and the spin-orbit scattering parameter (λ_{SO}), so that the doping-induced enhancement of λ_{SO} can also be obtained. The detailed analysis of the data using WHH model is presented in the Supplemental Material [47] (see also Ref. [63] therein). As depicted in Fig. S4 in the Supplemental Material [47], there are deviations of the data points from this one-band WHH model due to an upward curvature with a concave shape in the $H_{c2}(T)$ curve. This type of upward curvature has been reported for many of the iron arsenide superconductors, which has been attributed to the multiband effect [65,66]. Our attempts to fit the data with an effective two-band model [67] were not decisive, as they resulted in a high uncertainty of the parameter values and therefore were not included in this report. Additionally, the fitting of the one-band WHH model resulted in a large value of α_M, which does not satisfy Eq. (5), though we find an apparent enhancement in the λ_{SO} due to the substitution of heavier elements Ir and Rh with respect to Ru (please see Table S3 in the Supplemental Material [47]).

D. Specific heat

The temperature-dependent specific heat measurements on $LaRu_3Si_2$, $La(Ru_{1-x}Ir_x)_3Si_2$ ($x = 0$, 0.05, and 0.1), and $La(Ru_{1-y}Rh_y)_3Si_2$ ($y = 0$, 0.05, and 0.1) samples were performed in zero and various applied fields. Considering the presence of Ru (∼15%) as an extra phase in the samples studied, we have applied a small correction 0.47 mJ mole^{-1} K^{-2} to the measured raw data [24]. Furthermore, it is justified to ignore the contribution of the superconducting phase of Ru, as it is comparatively much lower than the temperature range used in this paper [68]. Figures 7(a) and 7(b) show the (corrected) specific heat divided by temperature (C/T) as a function of temperature in the T range 1.8–20 K. A pronounced anomaly in the zero-field C/T data of all these samples demonstrates the onset of bulk superconductivity. We employed idealized equal entropy constructions around the superconducting transition to determine T_c [e.g., the inset of Fig. 7(a) shows one such construction]. For all these compounds, we find the T_c obtained from C data is comparatively lower than the values deduced from resistivity and magnetization measurements. Such a difference in the estimated T_c values is generally observed in polycrystalline samples [69]. As already mentioned in the magnetization and resistivity analysis, it is consistent that the rate of decrease of T_c with the Rh concentration is higher than that of the Ir concentration. Figure 7(c) presents the systematic shifting of the superconducting peak by increasing the applied magnetic field. One may also notice that the characteristic peak in the C/T vs T plot of the doped samples gets broadened with

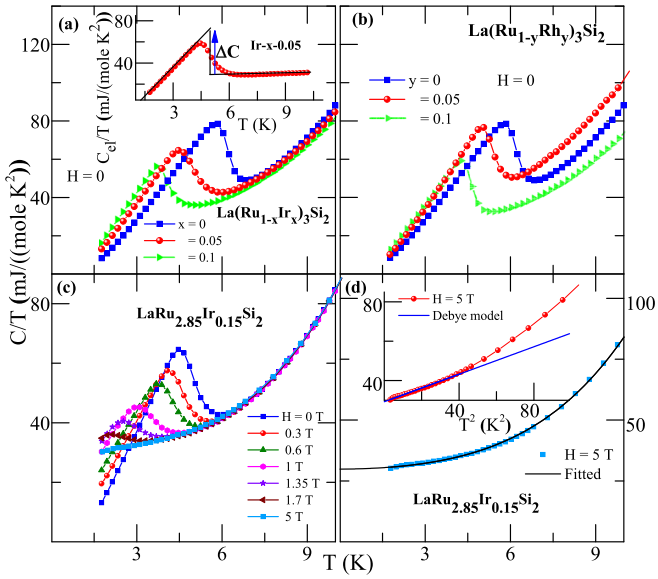

FIG. 7. The raw data of specific heat in terms of C/T vs T graph for (a) $La(Ru_{1-x}Ir_x)_3Si_2$ and (b) $La(Ru_{1-y}Rh_y)_3Si_2$. (c) Temperature dependence of C/T of $LaRu_{2.85}Ir_{0.15}Si_2$ measured in the presence of magnetic fields from 0 to 5 T (including Ru correction). (d) Temperature dependence of C/T of $LaRu_{2.85}Ir_{0.15}Si_2$ measured in an applied field of 5 T. The solid line through the data points shows the fit of the equation as described in the text. Inset (d) shows the plot between C/T vs T^2 of $LaRu_{2.85}Ir_{0.15}Si_2$.

the application of a magnetic field, like that of the pristine, which might be related to anisotropy of the upper critical field [$H_{c2}(0)$] and/or to the superconducting fluctuations [24]. In an applied field of 50 kOe, the superconductivity in these compounds is completely suppressed, or the transition has been shifted <1.8 K (temperature limitation of our system), and thus C_{5T} data were used for the characterization of the normal state behavior. The inset of Fig. 7(d) shows the $C_N(T)/T$ vs T^2 plot <15 K, which is nonlinear, implying the additional contribution of low-lying phonon modes. Therefore, the normal state C data were fitted with the following equation: $C_N(T) = \gamma_n T + \beta T^3 + \delta T^5$, comprising the electronic specific heat ($\gamma_n T$) and phonon specific heat ($\beta T^3 + \delta T^5$) [70]. One such fitting is illustrated in the main panel of Fig. 7(d). Table I summarizes the coefficients γ_n, β, and δ obtained from this fit for all compositions. It is worth noting that the coefficients of the electronic and phonon-specific heat of the parent sample are in reasonable agreement with the values provided by Li *et al.* [24]. As evident from the table, the Sommerfeld coefficient (γ_n) exhibits a marginal decrease with Rh/Ir substitution from 33.3 mJ mole^{-1} K^{-2} for $x(y) = 0$ x to 25.2 (25.5) mJ mole^{-1} K^{-2} for $x(y) = 0.1$, though these values are still much higher than that of simple metals, implying strong electronic correlation and relatively large effective mass of the carriers. Moreover, the Debye temperature of each of the compounds was estimated using the relation derived from the simple Debye model as follows:

$$\theta_D = \left(\frac{12\pi^4 NR}{5\beta}\right)^{1/3},$$

where N is the number of atoms in the formula unit and R is the gas constant. The θ_D values thus obtained are also shown in Table I, which decreases with the increase in the doping concentration. Acquiring the values of θ_D enables us to calculate the electron-phonon coupling constant ($\lambda_{el\text{-}ph}$), which is a dimensionless parameter characterizing the strength of attractive interaction between the electrons via phonons. We used the inverted McMillan's formula to evaluate $\lambda_{el\text{-}ph}$ as shown below [71]:

$$\lambda_{e\text{-}ph} = \frac{1.04 + \mu^* \ln\left(\frac{\theta_D}{T_c}\right)}{(1 - 0.62\mu^*)\ln\left(\frac{\theta_D}{T_c}\right) - 1.04}, \quad (6)$$

where μ^* is a material-dependent parameter, also known as the repulsive screened Coulomb parameter, having a value between 0.1 and 0.15. For metallic samples, μ^* is usually 0.13. With these considerations, we obtained the resultant $\lambda_{el\text{-}ph}$ in the range 0.66–0.58 (as shown in Table III), indicating intermediately coupled superconductivity in $LaRu_3Si_2$ and its doped variants.

Next, we estimated the noninteracting density of states at the Fermi level using its relationship with the Sommerfeld coefficient derived from the normal state electronic heat capacity:

$$\gamma_n = \frac{\pi^2 k_B^2}{3} N(E_F). \quad (7)$$

A comparison of the density of states of the doped samples with that of the pristine (please see Table III) shows a decrease of the density of states by increasing the Rh/Ir doping concentration. This is indicative of some sort of reconstruction of the Fermi surface induced by doping. In general, there is an enhancement of bare (band structure) density of states and bare effective mass caused by many-body electron-phonon interactions, and the corrections are as follows [72]:

$$N(E_F) = N_{band}(E_F)(1 + \lambda_{el\text{-}ph}), \quad (8)$$

$$m^* = m_{band}(1 + \lambda_{el\text{-}ph}). \quad (9)$$

Based on these equations and the obtained $N(E_F)$ values, we found $N_{band}(E_F)$ values in the range 7–9 states eV^{-1} f.u.$^{-1}$, which seems to corroborate the calculated band structure of the pristine [29] and is comparable with many of the metallic superconductors [73]. Because of the intermediate el-ph coupling constant, the effective mass m^* attains a value $\sim 1.6\, m_e$.

Since electronic specific heat contains striking features of the superconducting gap structure, we have shown C_{el}/T as a function of T/T_c for all studied samples in Figs. 8(a)–8(e). Here, C_{el}/T was obtained by subtracting the lattice contribution ($\beta T^3 + \delta T^5$) from the total measured heat capacity. Using the normal state γ_n values, we calculated the normalized specific heat jump at T_c, $\Delta C_{el}/\gamma_n T_c$, which turned out to be 1.47 ± 0.01, 1.45 ± 0.007, 1.46 ± 0.004, 1.58 ± 0.007, and 1.56 ± 0.01 for $x = 0$, 0.05 (Ir), 0.1 (Ir), 0.05 (Rh), and 0.1 (Rh), respectively. Consequently, this parameter is higher than the BCS value of 1.43 and hence indicates intermediately coupled superconductivity in this system, consistent with the results of $\lambda_{el\text{-}ph}$. A similar specific heat jump has been reported for $CuIr_{1.95}Ru_{0.05}Te_4$ [48], Re_6Zr [74], $Nb_{0.18}Re_{0.82}$ [49], $Nb_5Ir_{1.4}Pt_{1.6}O$ [75], and $Ba(Fe_{1-x}Co_x)_2As_2$ [76], which

TABLE III. Superconducting and normal state physical parameters of $La(Ru_{1-x}Ir_x)_3Si_2$ and $La(Ru_{1-y}Rh_y)_3Si_2$ (x, $y = 0$, 0.05, and 0.1) derived from the analysis of electronic specific heat. The calculated parameters $N(E_F)$, $N_{band}(E_F)$, and $\lambda_{el\text{-}ph}$ were derived using Eqs. (7), (8), and (6), respectively. The parameters $\frac{\Delta(0)}{k_B T_c}$ and γ_r were derived from the fitting of the α model [Eq. (14)].

Sample→		$La(Ru_{1-x}Ir_x)_3Si_2$			$La(Ru_{1-x}Rh_x)_3Si_2$	
Property↓	Unit↓	$x = 0$	$x = 0.05$	$x = 0.1$	$x = 0.05$	$x = 0.1$
T_c^*	K	6.3 ± 0.04	5.1 ± 0.05	4.2 ± 0.04	5.4 ± 0.05	4.55 ± 0.03
Θ_D	K	438 ± 11	366 ± 4	324 ± 2	291 ± 2	387 ± 5
$N(E_F)$	eV^{-1} f.u.$^{-1}$	14.15 ± 0.01	12.68 ± 0.06	10.72 ± 0.04	12.29 ± 0.07	10.82 ± 0.07
$N_{band}(E_F)$	eV^{-1} f.u.$^{-1}$	8.77 ± 0.01	7.89 ± 0.03	6.72 ± 0.03	7.4 ± 0.04	6.84 ± 0.04
λ_{el-ph}		0.61 ± 0.004	0.61 ± 0.005	0.59 ± 0.005	0.66 ± 0.004	0.58 ± 0.001
γ_n	mJ mole^{-1} K^{-2}	33.33 ± 0.23	29.88 ± 0.15	25.25 ± 0.09	28.96 ± 0.16	25.49 ± 0.17
$\frac{\gamma_r}{\gamma_n}$	%	10.5 ± 0.08	13.4 ± 0.08	19.8 ± 0.07	10.35 ± 0.06	17.65 ± 0.12
$\frac{\Delta C}{\gamma_0 T_c}$		1.47 ± 0.01	1.45 ± 0.007	1.46 ± 0.004	1.58 ± 0.007	1.56 ± 0.01
$\frac{\Delta(0)}{k_B T_c}$		1.88 ± 0.04	1.90 ± 0.03	1.98 ± 0.03	1.95 ± 0.04	1.98 ± 0.02
$\Delta(0)$	meV	1.02 ± 0.02	0.83 ± 0.01	0.71 ± 0.01	0.90 ± 0.02	0.77 ± 0.01

were also termed as intermediately coupled superconductors. Considering a flattening low-temperature behavior (as previously reported, Ref. [24]) and a small deviation from the weakly coupled BCS type system, we have analyzed the C_{el}/T data based on the α model, which has been derived from BCS theory but modified to consider the strong coupling, gap

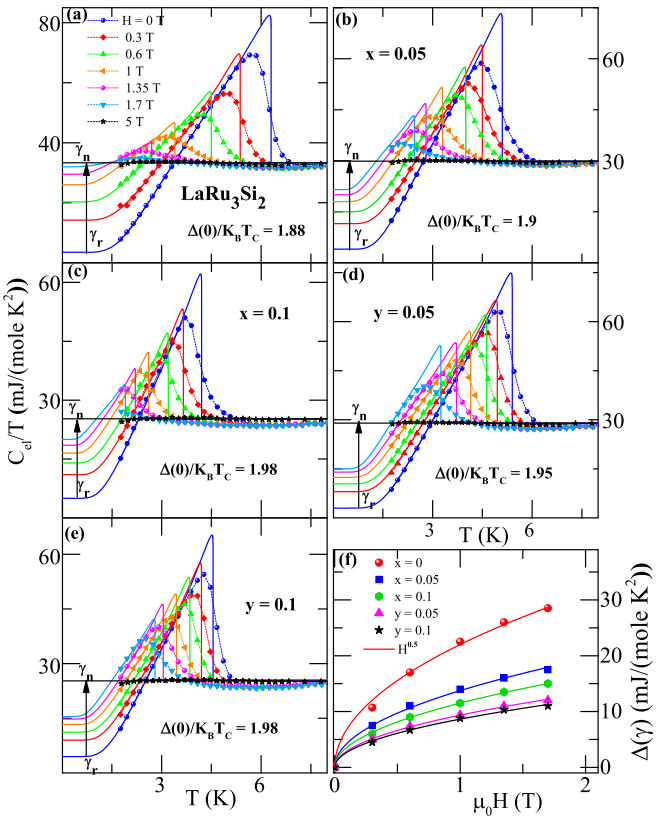

FIG. 8. C_{el}/T vs T graph for (a) $LaRu_3Si_2$, (b) $LaRu_{2.85}Ir_{0.15}Si_2$, (c) $LaRu_{2.7}Ir_{0.3}Si_2$, (d) $LaRu_{2.85}Rh_{0.15}Si_2$, and (e) $LaRu_{2.7}Ir_{0.3}Si_2$ in the presence of magnetic fields from 0 to 5 T. The solid lines represent the fitting curve using the modified Bardeen-Cooper-Schrieffer (BCS) model as described in the text. (f) The field dependence of reduced electronic specific heat coefficient $\Delta\gamma_r$.

anisotropy, multiple bands, and other aspects [77,78]. Within the framework of this α model, the entropy contribution from the superconductivity evolves with temperature as given below:

$$\frac{S}{\gamma_n T_c} = -\frac{6}{\pi^2}\left[\frac{\Delta(0)}{k_B T_c}\right]\int_0^\infty [f \ln f + (1-f)\ln(1-f)]dy, \tag{10}$$

where γ_n is the normal state Sommerfeld coefficient, f is the Fermi-Dirac distribution function and is expressed as a function of electronic energy as follows: $f(\xi) = \exp\{[\frac{E(\xi)}{k_B T}] + 1\}^{-1}$. The normalized superconducting entropy (S) is generally calculated over the entire energy range of electrons. The energy of the quasiparticles (paired states) according to BCS theory is

$$E(\xi) = \sqrt{\xi^2 + \Delta(t)^2}, \tag{11}$$

with $\xi = \frac{y}{\Delta(0)}$ and $t = \frac{T}{T_c}$. While the superconducting energy gap $\Delta(t)$ varies with temperature following the relation as given below:

$$\Delta(t) = \Delta(0)\tanh\left(1.82\left\{1.082\left[\left(\frac{1}{t}\right) - 1\right]\right\}^{0.51}\right), \tag{12}$$

the electronic specific heat of the superconducting state can be calculated from the normalized entropy by using the mathematical relation as

$$\frac{C_{es}}{\gamma_n T_c} = t\,\frac{d\left(\frac{S}{\gamma_n T_c}\right)}{dt}. \tag{13}$$

Though we find a satisfactory agreement between the experimental data and Eq. (13) with a saturating feature as T tends to 0 K, the extrapolated value of C_{es}/T in zero fields is finite and nonzero, which may be designated as the residual electronic specific heat coefficient (γ_r). This finite γ_r in zero fields indicates the presence of either a small fraction of nonsuperconducting carriers/quasiparticles or nodal quasiparticles from the nodal superconducting gap. With this consideration, we fitted our experimental C_{es}/T with the α

model by adding an extra term ($\gamma_r T$) and normalizing C_{es} as described below [79]:

$$\frac{C_{es}}{(\gamma_n - \gamma_r)T_c} = t\,\frac{d\left[\frac{S}{(\gamma_n-\gamma_r)T_c}\right]}{dt}. \tag{14}$$

Furthermore, we considered α [$=\Delta(0)/k_B T_c$] and γ_r as variable parameters during the fit. Figure 8 shows the excellent agreement of the C_{es}/T of the pristine as well as the doped samples with Eq. (14). The parameters obtained from the best fit are summarized in Table III. It may be noted that the value of γ_r is $\sim$3.5 mJ mole^{-1} K^{-2} for the parent sample $LaRu_3Si_2$, giving rise to the ratio of γ_r/γ_n as 10.5%. Since we have already eliminated the contribution of the additional Ru phase and the normal state Sommerfeld coefficient, such a fraction of γ_r is not expected, although a similar analysis of the heat capacity data of the doped samples yields an enhanced γ_r (with doping level) irrespective of Ir or Rh doping (shown in Table III) as if the nonsuperconducting quasiparticles increased with the doping level.

To extract more information related to the nature of these quasiparticle excitations, we analyze the C_{es}/T behavior at various applied magnetic fields and examined the field dependence of $\Delta\gamma_r[=\gamma_r(H) - \gamma_r(0)]$. The obtained results are presented in the inset of Fig. 8(f). For a conventional nodeless s-wave superconductor, the $\Delta\gamma_r$ is expected to vary linearly with the applied field, whereas a square root dependence with the field is shown for a d-wave superconductor [80]. Considering the apparent deviation of $\Delta\gamma_r(H)$ from linear field dependence, we fitted the data with a power law behavior [$\Delta\gamma_r = R(\mu_0 H)^n$, where R and n are the fitting parameters]. For all samples, we find a $\sqrt{H}$ dependence of $\Delta\gamma_r$, suggesting the presence of an anisotropic gap structure. A previous study on electronic heat capacity of the parent compound has also reported nonlinear H dependence of the quasiparticle excitations, though it was not conclusively a square root dependent behavior. Though the results of the La-NQR study have shown s-wave type behavior of the parent compound, a linear field dependence of $\Delta\gamma_r$ was not obtained. It may also be noted that the linear dependence of $\Delta\gamma_r$ is expected only above the lower critical field, as vertex interaction may give rise to some sort of curvature around $H_{c1}(0)$, as shown for the s-wave superconductor V_3Si [81]. On the other hand, the low-T (T close to zero) specific heat data exhibit an apparent flattening behavior, which is seemingly in contrast to the d-wave pairing symmetry of the order parameter. Moreover, theoretical studies of d-wave superconductors have pointed out that the Doppler shift of the quasiparticle excitation spectrum around the nodes modifies the density of states and gives rise to a $\sqrt{H}$ dependence of $\Delta\gamma_r$ and is valid only at the clean limit of the superconductor [79,82]. On the other hand, if the field dependence of $\Delta\gamma_r$ arises due to impurity scattering effects as expected in the dirty limit of a d-wave superconductor, $\Delta\gamma_r$ should vary as $H \log H$ in the low field limit ($H_{c1} < H < H_{c2}$) [83]. However, we did not get a proper $H \log H$ dependence of $\Delta\gamma_r$ even though the electronic properties of these samples (discussed in the next section) establish the observed superconductivity in the dirty limit of the specimens.

Alternatively, $\sqrt{H}$ dependence of $\Delta\gamma_r$ has also been observed in many other superconductors with multiband features such as $TlNi_2Se_2$ [84] and $Ta_4Pd_3Te_{16}$ [85]. A recent report on the band structure calculation of the parent $LaRu_3Si_2$ has shown a complex three-dimensional Fermi surface with contribution from several bands, suggesting a multiband feature [29]. Therefore, the nonlinear contribution of $\Delta\gamma_r$ may be attributed to the multiband effects.

The fitting of the α model also yielded the superconducting gap parameter [$\alpha = \Delta(0)/k_B T$], which apparently increases with increasing the doping concentration. The gap parameter, which characterizes the superconducting state, has a direct correlation with the electron-phonon coupling constant in the phonon mediated superconductivity. However, in these samples, $\lambda_{el\text{-}ph}$ does not show any substantial variation with doping.

E. Electronic properties of the superconducting state

Next, we determined some of the important superconducting properties of $LaRu_3Si_2$ and its doped variants by assembling the results of magnetization, resistivity, and heat capacity. The obtained values of $\mu_0 H_{c2}(0)$ and $\mu_0 H_{c1}(0)$ were used to calculate the GL coherence length $\xi_{GL}(0)$ and penetration depths $\lambda_{GL}(0)$ by employing the following equations:

$$\mu_0 H_{c2}(0) = \frac{\Phi_0}{2\pi\xi^2_{GL}(0)}, \tag{15}$$

where $\Phi_0 (= h/2e = 2.07 \times 10^{-3}\ \mathrm{T\,\mu m^2})$ is the magnetic flux quantum, and

$$\mu_0 H_{c1}(0) = \frac{\Phi_0}{4\pi\lambda^2_{GL}(0)} \ln\frac{\lambda_{GL}(0)}{\xi_{GL}(0)}. \tag{16}$$

Subsequently, the GL parameter is obtained as $\kappa = \frac{\lambda_{GL}(0)}{\xi_{GL}(0)}$, which signifies the type (either I or II) of superconductivity. Considering the dirty limit conditions of the samples, the GL parameter κ_0 (in the clean limit) can be obtained by using the Gorkov-Goodman relation as follows:

$$\kappa = \kappa_0 + 2.37 \times 10^6 \gamma^{1/2} \rho_0. \tag{17}$$

Moreover, the critical thermodynamic field is calculated using the values of $\xi_{GL}(0)$ and $\lambda_{GL}(0)$ following the relation given below:

$$H_{c1}\ (0) H_{c2}(0) = H_c^{cal}(0)^2 \ln\kappa. \tag{18}$$

All physical parameters $\xi_{GL}(0)$, $\lambda_{GL}(0)$, κ, κ_0, and $H_c^{cal}(0)$ as derived by using the above mentioned relations are summarized in Table IV. With the values of $\xi_{GL}(0)$ in the range 8–9 nm and $\lambda_{GL}(0)$ in the range 130–150 nm, we attain κ_0 as 12–20 ($\gg \frac{1}{\sqrt{2}}$) categorizing these samples to strongly type-II superconductors.

To obtain a self-consistency check on the derived parameters, we calculated the superconducting condensation energy (U_C) by integrating the entropy difference between the normal and superconducting states, given by the following expression:

$$U_C = \int_0^{7K} \Delta S(T) dT, \quad \text{where} \quad \Delta S(T) = \int_0^T \frac{\Delta C(T')}{T'} dT'. \tag{19}$$

TABLE IV. Comparison of the derived electronic properties of $La(Ru_{1-x}Ir_x)_3Si_2$ and $La(Ru_{1-y}Rh_y)_3Si_2$ (x, $y = 0$, 0.05, and 0.1). The parameters $\lambda_{GL}(0)$, ξ_0, v_F, and κ_0 were obtained from Eqs. (23), (24), (22), and (17), respectively.

Sample→		$La(Ru_{1-x}Ir_x)_3Si_2$			$La(Ru_{1-x}Rh_x)_3Si_2$	
Property↓	Unit↓	$x = 0$	$x = 0.05$	$x = 0.1$	$x = 0.05$	$x = 0.1$
$\lambda_{GL}(0)$	nm	135 ± 1	161 ± 1	145 ± 1	137 ± 1	129 ± 2
N	10^{28} m^{-3}	4.33 ± 0.09	2.30 ± 0.03	1.11 ± 0.01	2.42 ± 0.03	1.31 ± 0.01
ξ_0	nm	98.7 ± 0.8	120 ± 1	145 ± 1	137 ± 1	139 ± 0.8
l	nm	1.03 ± 0.01	0.652 ± 0.003	0.569 ± 0.004	0.636 ±0.006	0.748 ± 0.014
$\frac{\xi_0}{l}$		95.8 ± 0.2	184.7 ± 0.2	254.83 ±0.04	215.4 ± 0.4	185.8 ± 1.4
v_F	10^4 ms^{-1}	12.76 ± 0.09	9.34 ± 0.05	6.79 ± 0.03	9.91 ± 0.04	7.47 ± 0.15
κ		14.84 ± 0.02	20.1 ± 0.02	16.29 ± 0.04	16.1 ± 0.1	14.1 ± 0.14
κ_0		14.4 ± 0.02	19.1 ± 0.02	14.59 ± 0.04	15.3 ± 0.1	12.84 ± 0.14

This analysis yields the condensation energy of 275.3, 162.9, and 97.4 mJ/mole for $La(Ru_{1-x}Ir_x)_3Si_2$ samples with $x = 0$, 0.05, and 0.1, respectively, and 191.9 and 119.1 mJ/mole for $La(Ru_{1-y}Rh_y)_3Si_2$ with $y = 0.05$ and 0.1, respectively.

Here, U_C can also be determined from the zero-field superconducting gap and electronic specific heat coefficient as follows [86]:

$$U_C = gN(E_F)\frac{\Delta(0)^2}{2} = g\frac{3}{4\pi^2}\frac{1}{k_B^2}\gamma_n\Delta(0)^2. \quad (20)$$

For a BCS superconductor, $g = 1$, $\Delta(0) = \alpha k_B T_c$. Using Eq. (20), we obtain the values of condensation energy as 355, 213, and 133 mJ/mole for the pristine, 5%, and 10% Ir-doped samples, while it is 244 and 157 mJ/mole for 5% and 10% Rh-doped samples.

The thermodynamic critical field [$H_c(0)$] is directly related to the free energy difference of the normal and superconducting states and therefore can be evaluated from the condensation energy using the following the expression:

$$\frac{1}{2}\mu_0 H_c^{ex}(0)^2 = U_C. \quad (21)$$

The critical fields [$H_c^{cal}(0)$] obtained by using the above Eq. (18) are in good agreement with the experimental results [$H_c^{ex}(0)$] derived from Eq. (21) (see Table II).

To further explore the electronic properties of these materials, we estimated the Fermi velocity (v_F), which is related to the density of states as follows:

$$v_F = \frac{\pi^2\hbar^3}{m^{*2}V_{f.u.}}N(E_F), \quad (22)$$

where m^* is the effective mass, $\hbar$ is Planck's constant, k_B is the Boltzmann constant, and $V_{f.u.} = V_{cell}/2$ is the volume of the formula unit. Using the values of m^*, γ_n, and $V_{f.u.}$, we obtained the Fermi velocity of the order of 6.8–12.8 × 10^4 m/s. Furthermore, we estimated the mean free path (l) of the superconducting carriers by using the relation $l = v_F\tau$, where the mean free scattering time, $\tau = \frac{m^*}{n_s e^2\rho_0}$ (ρ_0 is the residual resistivity, and n_s is the superconducting carrier density). Assuming a spherical Fermi surface [87], n can be expressed as $n = \frac{m^{*3}v_F^3}{3\pi^2\hbar^3}$. The obtained values of n lie in the range 1×10^{28} to 4×10^{28} m^{-3}, which is like other metallic superconductors [49,73,74]. Combining all the above expressions, we derived the mean free path of the charge carriers in the studied samples using the expression $l = 3\pi^2(\frac{\hbar}{e^2\rho_0})(\frac{\hbar}{m^*v_F})^2$, which turned out to be in the range 4–10 nm. It is apparent from the comparison that the mean free path being lower than the respective GL coherence length indicates the observed superconductivity in the dirty limit.

In the dirty limit, the GL penetration depth and coherence length get affected and can be expressed by the following modified Eqs. (23) and (24), respectively:

$$\lambda_{GL}(0) = \lambda_L\left(1 + \frac{\xi_0}{l}\right)^{1/2}, \quad (23)$$

where ξ_0 is the BCS coherence length and λ_L is the London penetration depth, and

$$\frac{\xi_{GL}(0)}{\xi_0} = \frac{\pi}{2\sqrt{3}}\left(1 + \frac{\xi_0}{l}\right)^{-1/2}. \quad (24)$$

Finally, we have estimated the effective Fermi temperature using the derived values of m^* and n using the following relation [88]:

$$k_B T_F = \frac{\hbar^2}{2m^*}(3\pi^2 n)^{2/3}. \quad (25)$$

In Table IV, we have summarized all estimated electronic parameters. Using these parameters, we have calculated the ratio T_c/T_F which turned out to be ∼0.002 for the parent compound and ∼0.005 for the 10% doped samples. However, since these calculations have been carried out by considering the simplified version of the Fermi surface (spherical Fermi surface), any deviations may arise when Fermi surface anisotropy and multiband effects are included.

IV. SUMMARY

In summary, we have successfully synthesized the polycrystalline samples of $La(Ru_{1-x}Ir_x)_3Si_2$ ($x = 0$, 0.05, and 0.1) and $La(Ru_{1-y}Rh_y)_3Si_2$ ($y = 0.05$ and 0.1) to study the effect of substituting a high SOC element at the Ru site on the normal and superconducting properties of the distorted kagome lattice compound $LaRu_3Si_2$. Rietveld analyses of the PXRD data confirm all solid solutions to crystallize in the same distorted structure in the space group $P6_3/mmc$ with a small lattice compression for Rh-doped samples. The results of magnetic susceptibility, electrical resistivity, and heat

capacity measurements establish type-II bulk superconductivity in all compositions with moderate el-ph coupling. The superconducting transition temperature obtained from $\chi(T)$, $\rho(T)$, or $C(T)$ data shows a gradual suppression with the doping concentration (Ir or Rh), while the rate of suppression is marginally higher for Rh-doped samples. This decrease in T_c is consistent with the decrease in the density of states, estimated from the coefficient of the electronic heat capacity data. However, a significant enhancement of the upper critical value $[H_{c2}(0)]$ was observed for Ir substitution in comparison with that of Rh substitution (at low doping level) possibly related to the effective SOC of the system. The characteristic length scales and the corresponding Maki parameter indicate the dominance of the orbital pair-breaking effect. Our analyses of the electronic specific heat of the superconducting state can be well fitted to a model with a single-band isotropic gap, while the change of the residual electronic specific heat coefficient induced by magnetic field varies as the square root of the applied field. With the characteristic feature of the electronic specific heat as *s*-wave type, the nonlinear dependence of γ_r can be attributed to the multiband effect. The normalized heat capacity jump $\frac{\Delta C}{\gamma_n T_c}$ and the gap parameter $\frac{2\Delta_0}{k_B T_c^*}$ suggest moderately coupled superconductivity with an increase in the gap parameter induced by doping.

[1] S. Sachdev, Kagomé-and triangular-lattice Heisenberg antiferromagnets: Ordering from quantum fluctuations and quantum-disordered ground states with unconfined bosonic spinons, Phys. Rev. B **45**, 12377 (1992).

[2] T. H. Han, J. S. Helton, S. Chu, D. G. Nocera, J. A. Rodriguez-Rivera, C. Broholm, and Y. S. Lee, Fractionalized excitations in the spin-liquid state of a kagome-lattice antiferromagnet, Nature (London) **492**, 406 (2012).

[3] M. Kang, L. Ye, S. Fang, J.-S. You, A. Levitan, M. Han, J. I. Facio, C. Jozwiak, A. Bostwick, and E. Rotenberg, Dirac fermions and flat bands in the ideal kagome metal FeSn, Nat. Mater. **19**, 163 (2020).

[4] L. Ye, M. Kang, J. Liu, F. von Cube, C. R. Wicker, T. Suzuki, C. Jozwiak, A. Bostwick, E. Rotenberg, and D. C. Bell, Massive Dirac fermions in a ferromagnetic kagome metal, Nature (London) **555**, 638 (2018).

[5] H. M. Guo and M. Franz, Topological insulator on the kagome lattice, Phys. Rev. B **80**, 113102 (2009).

[6] A. O'Brien, F. Pollmann, and P. Fulde, Strongly correlated fermions on a kagome lattice, Phys. Rev. B **81**, 235115 (2010).

[7] S. Yan, D. A. Huse, and S. R. White, Spin-liquid ground state of the $S = \frac{1}{2}$ kagome Heisenberg antiferromagnet, Science **332**, 1173 (2011).

[8] L. Balents, Spin liquids in frustrated magnets, Nature (London) **464**, 199 (2010).

[9] M. Fu, T. Imai, T. H. Han, and Y. S. Lee, Evidence for a gapped spin-liquid ground state in a kagome Heisenberg antiferromagnet, Science **350**, 655 (2015).

[10] S. K. Upadhyay, K. K. Iyer, and E. V. Sampathkumaran, Magnetic behavior of metallic kagome lattices, $Tb_3Ru_4Al_{12}$ and $Er_3Ru_4Al_{12}$, J. Phys.: Condens. Matter **29**, 325601 (2017).

[11] V. Chandragiri, K. K. Iyer, and E. V. Sampathkumaran, Insight into the magnetism of a distorted kagome lattice, $Dy_3Ru_4Al_{12}$, based on polycrystalline studies, Intermetallics **76**, 26 (2016).

[12] M. Kang, S. Fang, L. Ye, H. C. Po, J. Denlinger, C. Jozwiak, A. Bostwick, E. Rotenberg, E. Kaxiras, and J. G. Checkelsky, Topological flat bands in frustrated kagome lattice CoSn, Nat. Commun. **11**, 4004 (2020).

[13] C. D. O'Neill, A. S. Wills, and A. D. Huxley, Possible topological contribution to the anomalous Hall effect of the noncollinear ferromagnet Fe_3Sn_2, Phys. Rev. B **100**, 174420 (2019).

[14] E. Liu, Y. Sun, N. Kumar, L. Muechler, A. Sun, L. Jiao, S. Y. Yang, D. Liu, A. Liang, Q. Xu *et al.*, Giant anomalous Hall effect in a ferromagnetic kagome-lattice semimetal, Nat. Phys. **14**, 1125 (2018).

[15] J. X. Yin, S. S. Zhang, G. Chang, Q. Wang, S. S. Tsirkin, Z. Guguchia, B. Lian, H. Zhou, K. Jiang, I. Belopolski *et al.*, Negative flat band magnetism in a spin–orbit-coupled correlated kagome magnet, Nat. Phys. **15**, 443 (2019).

[16] D. F. Liu, A. J. Liang, E. K. Liu, Q. N. Xu, Y. W. Li, C. Chen, D. Pei, W. J. Shi, S. K. Mo, P. Dudin *et al.*, Magnetic Weyl semimetal phase in a kagomé crystal, Science **365**, 1282 (2019).

[17] A. Rüegg and G. A. Fiete, Fractionally charged topological point defects on the kagome lattice, Phys. Rev. B **83**, 165118 (2011).

[18] I. I. Mazin, H. O. Jeschke, F. Lechermann, H. Lee, M. Fink, R. Thomale, and R. Valentí, Theoretical prediction of a strongly correlated Dirac metal, Nat. Commun. **5**, 4261 (2014).

[19] B. R. Ortiz, S. M. L. Teicher, Y. Hu, J. L. Zuo, P. M. Sarte, E. C. Schueller, A. M. M. Abeykoon, M. J. Krogstad, S. Rosenkranz, and R. Osborn, CsV_3Sb_5: A $\mathbb{Z}_2$ Topological Kagome Metal with a Superconducting Ground State, Phys. Rev. Lett. **125**, 247002 (2020).

[20] K. S. Athreya, L. S. Hausermann-Berg, R. N. Shelton, S. K. Malik, A. M. Umarji, and G. K. Shenoy, Superconductivity in the ternary borides $CeOs_3B_2$ and $CeRu_3B_2$: Magnetic susceptibility and specific heat measurements, Phys. Lett. A **113**, 330 (1985).

[21] H. C. Ku, G. P. Meisner, F. Acker, and D. C. Johnston, Superconducting and magnetic properties of new ternary borides with the $CeCo_3B_2$-type structure, Solid State Commun. **35**, 91 (1980).

[22] U. Rauchschwalbe, W. Lieke, F. Steglich, C. Godart, L. C. Gupta, and R. D. Parks, Superconductivity in a mixed-valent system: $CeRu_3Si_2$, Phys. Rev. B **30**, 444 (1984).

[23] D. K. Misemer, S. Auluck, S. I. Kobayasi, and B. N. Harmon, Electronic structure of $LaRh_3B_2$ and $CeRh_3B_2$, Solid State Commun. **52**, 955 (1984).

[24] S. Li, B. Zeng, X. Wan, J. Tao, F. Han, H. Yang, Z. Wang, and H.-H. Wen, Anomalous properties in the normal and superconducting states of $LaRu_3Si_2$, Phys. Rev. B **84**, 214527 (2011).

[25] B. R. Ortiz, P. M. Sarte, E. M. Kenney, M. J. Graf, S. M. L. Teicher, R. Seshadri, and S. D. Wilson, Superconductivity in the $\mathbb{Z}_2$ kagome metal KV_3Sb_5, Phys. Rev. Mater. **5**, 034801 (2021).

[26] X. Wu, T. Schwemmer, T. Müller, A. Consiglio, G. Sangiovanni, D. Di Sante, Y. Iqbal, W. Hanke, A. P. Schnyder,

and M. M. Denner, Nature of Unconventional Pairing in the Kagome Superconductors AV_3Sb_5 (A = K, Rb, Cs), Phys. Rev. Lett. **127**, 177001 (2021).

[27] T. Neupert, M. Michael Denner, J.-X. Yin, R. Thomale, and M. Zahid Hasan, Charge order and superconductivity in kagome materials, Nat. Phys. **18**, 137 (2022).

[28] Y.-X. Jiang, J.-X. Yin, M. M. Denner, N. Shumiya, B. R. Ortiz, G. Xu, Z. Guguchia, J. He, M. S. Hossain, and X. Liu, Unconventional chiral charge order in kagome superconductor KV_3Sb_5, Nat. Mater. **20**, 1353 (2021).

[29] C. Mielke, Y. Qin, J. X. Yin, H. Nakamura, D. Das, K. Guo, R. Khasanov, J. Chang, Z. Q. Wang, S. Jia *et al.*, Nodeless kagome superconductivity in $LaRu_3Si_2$, Phys. Rev. Mater. **5**, 034803 (2021).

[30] D. J. Singh and M. H. Du, Density Functional Study of $LaFeAsO_{1-x}F_x$: A Low Carrier Density Superconductor Near Itinerant Magnetism, Phys. Rev. Lett. **100**, 237003 (2008).

[31] Y. Kishimoto, Y. Kawasaki, T. Ohno, L. C. Gupta, and G. Ghosh, La-NQR probe of strong-coupling s-wave superconductivity in $LaRu_3Si_2$, J. Phys. Soc. Jpn. **73**, 190 (2004).

[32] Y. Cao, V. Fatemi, S. Fang, K. Watanabe, T. Taniguchi, E. Kaxiras, and P. Jarillo-Herrero, Unconventional superconductivity in magic-angle graphene superlattices, Nature (London) **556**, 43 (2018).

[33] S. Majumdar and E. V. Sampathkumaran, Observation of enhanced magnetic transition temperature in Nd_2PdGe_3 and superconductivity in Y_2PdGe_3, Phys. Rev. B **63**, 172407 (2001).

[34] R. Kumar, K. K. Iyer, P. L. Paulose, and E. V. Sampathkumaran, Magnetic and transport anomalies in R_2RhSi_3 (R = Gd, Tb, and Dy) resembling those of the exotic magnetic material Gd_2PdSi_3, Phys. Rev. B **101**, 144440 (2020).

[35] P. W. Anderson, Theory of dirty superconductors, J. Phys. Chem. Solids **11**, 26 (1959).

[36] A. V. Balatsky, I. Vekhter, and J.-X. Zhu, Impurity-induced states in conventional and unconventional superconductors, Rev. Mod. Phys. **78**, 373 (2006).

[37] G. Xiao, M. Z. Cieplak, J. Q. Xiao, and C. L. Chien, Magnetic pair-breaking effects: moment formation and critical doping level in superconducting $La_{1.85}Sr_{0.15}Cu_{1-x}A_xO_4$ systems (A = Fe, Co, Ni, Zn, Ga, Al), Phys. Rev. B **42**, 8752 (1990).

[38] M. H. Julien, T. Fehér, M. Horvatic, C. Berthier, O. N. Bakharev, P. Ségransan, G. Collin, and J. F. Marucco, ^{63}Cu NMR Evidence for Enhanced Antiferromagnetic Correlations around Zn Impurities in $YBa_2Cu_3O_{6.7}$, Phys. Rev. Lett. **84**, 3422 (2000).

[39] P. Cheng, B. Shen, J. Hu, and H. H. Wen, Contrasting impurity scattering and pair-breaking effects by doping Mn and Zn in $Ba_{0.5}K_{0.5}Fe_2As_2$, Phys. Rev. B **81**, 174529 (2010).

[40] Q. Deng, X. Ding, S. Li, J. Tao, H. Yang, and H. H. Wen, The effect of impurity and the suppression of superconductivity in $Na(Fe_{0.97-x}Co_{0.03}T_x)As$ (T = Cu, Mn), New J. Phys. **16**, 063020 (2014).

[41] C. Godart and L. C. Gupta, Coexistence of superconductivity and spin glass freezing in $La_{0.95}Gd_{0.05}Ru_3Si_2$, Phys. Lett. A **120**, 427 (1987).

[42] M. Escorne, A. Mauger, L. C. Gupta, and C. Godart, Type-II superconductivity in a dilute magnetic system: $La_{1-x}Tm_xRu_3Si_2$, Phys. Rev. B **49**, 12051 (1994).

[43] S. Li, J. Tao, X. Wan, X. Ding, H. Yang, and H.-H. Wen, Distinct behaviors of suppression to superconductivity in $LaRu_3Si_2$ induced by Fe and Co dopants, Phys. Rev. B **86**, 024513 (2012).

[44] B. Li, S. Li, and H.-H. Wen, Chemical doping effect in the $LaRu_3Si_2$ superconductor with a kagome lattice, Phys. Rev. B **94**, 094523 (2016).

[45] Y. Wang, A. Kreisel, P. J. Hirschfeld, and V. Mishra, Using controlled disorder to distinguish $s_\pm$ and s_{++} gap structure in Fe-based superconductors, Phys. Rev. B **87**, 094504 (2013).

[46] J. Rodríguez-Carvajal, Recent advances in magnetic structure determination by neutron powder diffraction, Phys. B Condens. Matter **192**, 55 (1993).

[47] See Supplemental Material at http://link.aps.org/supplemental/10.1103/PhysRevB.107.024503 for data, calculation, and analysis.

[48] D. Yan, L. Zeng, Y. Lin, J. Yin, Y. He, X. Zhang, M. Huang, B. Shen, M. Wang, and Y. Wang, Superconductivity in Ru-doped $CuIr_2Te_4$ telluride chalcogenide, Phys. Rev. B **100**, 174504 (2019).

[49] S. Sundar, S. Salem-Sugui, M. K. Chattopadhyay, S. B. Roy, L. S. Sharath Chandra, L. F. Cohen, and L. Ghivelder, Study of $Nb_{0.18}Re_{0.82}$ non-centrosymmetric superconductor in the normal and superconducting states, Supercond. Sci. Technol. **32**, 055003 (2019).

[50] D. Y. Yan, M. Yang, C. X. Wang, P. B. Song, C. J. Yi, and Y. G. Shi, Superconductivity in centrosymmetric topological superconductor candidate TaC, Supercond. Sci. Technol. **34**, 035025 (2021).

[51] M. J. Winiarski, B. Wiendlocha, S. Gołąb, S. K. Kushwaha, P. Wiśniewski, D. Kaczorowski, J. D. Thompson, R. J. Cava, and T. Klimczuk, Superconductivity in $CaBi_2$, Phys. Chem. Chem. Phys. **18**, 21737 (2016).

[52] C. S. Yadav and P. L. Paulose, Upper critical field, lower critical field and critical current density of $FeTe_{0.60}Se_{0.40}$ single crystals, New J. Phys. **11**, 103046 (2009).

[53] M. Tinkham, *Introduction to Superconductivity* (McGraw Hill, New York, 1996).

[54] N. Zhou, X. Xu, J. R. Wang, J. H. Yang, Y. K. Li, Y. Guo, W. Z. Yang, C. Q. Niu, B. Chen, C. Cao, and J. Dai, Controllable spin-orbit coupling and its influence on the upper critical field in the chemically doped quasi-one-dimensional Nb_2PdS_5 superconductor, Phys. Rev. B **90**, 094520 (2014).

[55] M. Mandal, S. Marik, K. P. Sajilesh, Arushi, D. Singh, J. Chakraborty, N. Ganguli, and R. P. Singh, Enhancement of the superconducting transition temperature by Re doping in Weyl semimetal $MoTe_2$, Phys. Rev. Mater. **2**, 094201 (2018).

[56] S. Li, X. Liu, V. Anand, and B. Lv, Superconductivity from site-selective Ru doping studies in Zr_5Ge_3 compound, New J. Phys. **20**, 013009 (2018).

[57] G. Grimvall, *The Electron-Phonon Interaction in Metals* (North-Holland, Amsterdam, 1981).

[58] K. Kadowaki and S. B. Woods, Universal relationship of the resistivity and specific heat in heavy-fermion compounds, Solid State Commun. **58**, 507 (1986).

[59] Z. Fisk and G. W. Webb, Saturation of the High-Temperature Normal-State Electrical Resistivity of Superconductors, Phys. Rev. Lett. **36**, 1084 (1976).

[60] H. Wiesmann, M. Gurvitch, H. Lutz, A. Ghosh, B. Schwarz, M. Strongin, P. B. Allen, and J. W. Halley, Simple Model for Characterizing the Electrical Resistivity in $A-15$ Superconductors, Phys. Rev. Lett. **38**, 782 (1977).

[61] J. M. Ziman, *Electrons and Phonons: The Theory of Transport Phenomena in Solids* (Oxford University Press, Oxford, 2001).

[62] M. Deutsch, An accurate analytic representation for the Bloch-Gruneisen integral, J. Phys. A. Math. Gen. **20**, L811 (1987).

[63] N. R. Werthamer, E. Helfand, and P. C. Hohenberg, Temperature and purity dependence of the superconducting critical field, H_{c2}. III. electron spin and spin-orbit effects, Phys. Rev. **147**, 295 (1966).

[64] E. Helfand and N. R. Werthamer, Temperature and purity dependence of the superconducting critical field, H_{c2}. II, Phys. Rev. **147**, 288 (1966).

[65] F. Hunte, J. Jaroszynski, A. Gurevich, D. C. Larbalestier, R. Jin, A. S. Sefat, M. A. McGuire, B. C. Sales, D. K. Christen, and D. Mandrus, Two-band superconductivity in $LaFeAsO_{0.89}F_{0.11}$ at very high magnetic fields, Nature (London) **453**, 903 (2008).

[66] H. S. Lee, M. Bartkowiak, J. H. Park, J. Y. Lee, J. Y. Kim, N. H. Sung, B. K. Cho, C. U. Jung, J. S. Kim, and H. J. Lee, Effects of two gaps and paramagnetic pair breaking on the upper critical field of $SmFeAsO_{0.85}$ and $SmFeAsO_{0.8}F_{0.2}$ single crystals, Phys. Rev. B **80**, 144512 (2009).

[67] A. Gurevich, Enhancement of the upper critical field by nonmagnetic impurities in dirty two-gap superconductors, Phys. Rev. B **67**, 184515 (2003).

[68] B. B. Goodman, Two new superconducting elements, Nature (London) **167**, 111 (1951).

[69] L. C. Srivichitranond, E. M. Seibel, W. Xie, Z. Sobczak, T. Klimczuk, and R. J. Cava, Superconductivity in a new intermetallic structure type based on endohedral $Ta@Ir_7Ge_4$ clusters, Phys. Rev. B **95**, 174521 (2017).

[70] H. D. Yang and J.-Y. Lin, Low temperature specific heat studies on the pairing states of high-T_c superconductors: A brief review, J. Phys. Chem. Solids **62**, 1861 (2001).

[71] W. L. McMillan, Transition temperature of strong-coupled superconductors, Phys. Rev. **167**, 331 (1968).

[72] G. Grimvall, The electron-phonon interaction in normal metals, Phys. Scr. **14**, 63 (1976).

[73] D. Kumar, C. N. Kuo, F. Astuti, T. Shang, M. K. Lee, C. S. Lue, I. Watanabe, J. A. T. Barker, T. Shiroka, and L. J. Chang, Nodeless superconductivity in the cage-type superconductor $Sc_5Ru_6Sn_{18}$ with preserved time-reversal symmetry, J. Phys. Condens. Matter **30**, 315803 (2018).

[74] D. A. Mayoh, J. A. T. Barker, R. P. Singh, G. Balakrishnan, D. McK Paul, and M. R. Lees, Superconducting and normal-state properties of the noncentrosymmetric superconductor Re_6Zr, Phys. Rev. B **96**, 064521 (2017).

[75] Y. Xu, S. Jöhr, L. Das, J. Kitagawa, M. Medarde, T. Shiroka, J. Chang, and T. Shang, Crossover from multiple-to single-gap superconductivity in $Nb_5Ir_{3-x}Pt_xO$ alloys, Phys. Rev. B **101**, 134513 (2020).

[76] K. Gofryk, A. S. Sefat, E. D. Bauer, M. A. McGuire, B. C. Sales, D. Mandrus, J. D. Thompson, and F. Ronning, Gap structure in the electron-doped iron–arsenide superconductor $Ba(Fe_{0.92}Co_{0.08})_2As_2$: Low-temperature specific heat study, New J. Phys. **12**, 023006 (2010).

[77] H. Padamsee, J. E. Neighbor, and C. A. Shiffman, Quasiparticle phenomenology for thermodynamics of strong-coupling superconductors, J. Low Temp. Phys. **12**, 387 (1973).

[78] D. C. Johnston, Elaboration of the α-model derived from the BCS theory of superconductivity, Supercond. Sci. Technol. **26**, 115011 (2013).

[79] D. Campanini, Z. Diao, L. Fang, W.-K. Kwok, U. Welp, and A. Rydh, Superconducting gap evolution in overdoped $BaFe_2(As_{1-x}P_x)_2$ single crystals through nanocalorimetry, Phys. Rev. B **91**, 245142 (2015).

[80] G. E. Volovik, Superconductivity with lines of GAP nodes: Density of states in the vortex, JETP Lett. **58**, 469 (1993).

[81] A. P. Ramirez, Magnetic field dependent specific heat of V_3Si—downward curvature as a general feature of superconductivity, Phys. Lett. A **211**, 59 (1996).

[82] C. Kübert and P. J. Hirschfeld, Quasiparticle Transport Properties of d-Wave Superconductors in the Vortex State, Phys. Rev. Lett. **80**, 4963 (1998).

[83] C. Kübert and P. J. Hirschfeld, Vortex contribution to specific heat of dirty d-wave superconductors: breakdown of scaling, Solid State Commun. **105**, 459 (1998).

[84] H. Wang, C. Dong, Q. Mao, R. Khan, X. Zhou, C. Li, B. Chen, J. Yang, Q. Su, and M. Fang, Multiband Superconductivity of Heavy Electrons in a $TlNi_2Se_2$ Single Crystal, Phys. Rev. Lett. **111**, 207001 (2013).

[85] W. H. Jiao, Y. Liu, Y. K. Li, X. F. Xu, J. K. Bao, C. M. Feng, S. Y. Li, Z. A. Xu, and G. H. Cao, Multiband superconductivity in $Ta_4Pd_3Te_{16}$ with anisotropic gap structure, J. Phys.: Condens. Matter **27**, 325701 (2015).

[86] B. He, C. Dong, L. Yang, X. Chen, L. Ge, L. Mu, and Y. Shi, $CuNNi_3$: A new nitride superconductor with antiperovskite structure, Supercond. Sci. Technol. **26**, 125015 (2013).

[87] C. Kittel, *Introduction to Solid State Physics*, 8th ed. (Wiley, New York, 2005).

[88] Y. J. Uemura, L. P. Le, G. M. Luke, B. J. Sternlieb, W. D. Wu, J. H. Brewer, T. M. Riseman, C. L. Seaman, M. B. Maple, M. Ishikawa *et al.*, Basic Similarities among Cuprate, Bismuthate, Organic, Chevrel-Phase, and Heavy-Fermion Superconductors Shown by Penetration-Depth Measurements, Phys. Rev. Lett. **66**, 2665 (1991).